ACS APPLIED MATERIALS & INTERFACES

www.acsami.org Research Article

Ultramicroporous Metal−Organic Framework with Inert Pore Surfaces for Inversed Separation of Ethylene from C_2 Hydrocarbons Mixtures

Hai-Yu Duan, Xiu-Yuan Li,* Rajamani Krishna, and Chaozheng He*

Cite This: ACS Appl. Mater. Interfaces 2023, 15, 23538−23545

Read Online

ACCESS | Metrics & More | Article Recommendations | Supporting Information

ABSTRACT: The achievement of direct C_2H_4 separation from C_2 hydrocarbons is very challenging in the petrochemical industry due to their similar molecular sizes, boiling points, and physicochemical properties. In this work, a nonpolar/inert ultramicroporous metal−organic framework (MOF), $[Co_3(\mu_3\text{-}OH)(tipa)(bpy)_{1.5}]\cdot 3DMF\cdot 6H_2O$ (**1**), with stand-alone one-dimensional square tubular channels was successfully constructed, its pore enriched with plenty of aromatic rings causing nonpolar/inert pore surfaces. The MOF shows preferential adsorption of C_2H_6 compared to C_2H_4 and C_2H_2 in the low-pressure region, which is further verified by adsorption heats and selectivities. The C_2H_4 separation potential in one step for binary C_2H_6/C_2H_4 (50/50 and 10/90) and ternary $C_2H_4/C_2H_6/C_2H_2$ (89/10/1) is also examined by transient breakthrough simulations. Moreover, grand canonical Monte Carlo simulations demonstrate that the unique reversed adsorption mechanism is due to the shortest and most number of C−H···π interactions between C_2H_6 and the framework.

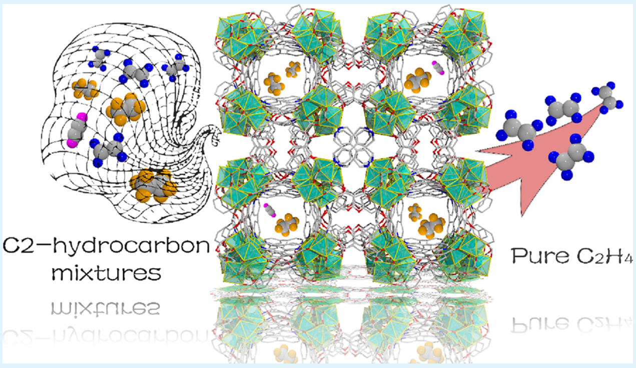

KEYWORDS: *metal−organic frameworks, inversed separation of ethylene, inert pore surfaces, GCMC simulations, breakthrough simulations*

1. INTRODUCTION

As one of the most important raw materials in the petrochemical industry,[1,2] C_2H_4 is widely used in producing synthetic fiber/plastic and other organic products.[3] However, some light hydrocarbon impurities, such as CH_4, C_2H_2, C_2H_6, and so on, are obtained along with C_2H_4 by a petroleum cracking process at high temperature.[4,5] Therefore, it is necessary to separate and purify C_2H_4 from the light hydrocarbon mixtures. Cryogenic distillation technology is a high energy consumption process in the chemical industry,[6−8] and it is difficult to separate C_2H_4 from C_2H_6 and C_2H_2 due to their similar molecular sizes, boiling points, and physicochemical properties.[9−12] Therefore, more effective and energy-saving separation methods need to be explored to replace traditional high energy-consuming methods.

The appearance of physical adsorbents is hopeful of greatly reducing the energy consumption of the purification process, which has the potential to replace traditional cryogenic distillation.[13−16] Metal−organic frameworks (MOFs) as novel porous materials can be precisely regulated and designed to obtain desired pore sizes and environments at the molecular level through crystal engineering approaches.[17−24] In general, most MOF materials exhibit the outstanding adsorption of unsaturated C_2 hydrocarbons with the relationship of adsorption capacities and affinity order of $C_2H_2 > C_2H_4 > C_2H_6$ because introducing open metal sites/clusters or polar groups on the pore surfaces of MOFs can give priority to binding molecules with high dipole and/or quadrupole moments (quadrupole moments of 7.2×10^{-26} esu cm^2 for C_2H_2, 1.5×10^{-26} esu cm^2 for C_2H_4, and 0.65×10^{-26} esu cm^2 for C_2H_6).[25−29] In addition, the kinetic diameter of C_2H_4 (4.163 Å) is between C_2H_6 (4.443 Å) and C_2H_2 (3.3 Å), so molecular sieving by adjusting the pore aperture cannot be implemented.[30] Therefore, the achievement of direct C_2H_4 separation in one step is a more challenging and desirable target[31−33] because high-purity C_2H_4 can be directly produced without an extra desorption step, thus avoiding a great deal of energy consumption. Compared with C_2H_4 and C_2H_2, C_2H_6 has the largest polarizability (39.3×10^{-25} cm^3 for C_2H_2; 42.52×10^{-25} cm^3 for C_2H_4; 44.7×10^{-25} cm^3 for C_2H_6), and

Received: March 27, 2023
Accepted: April 26, 2023
Published: May 8, 2023

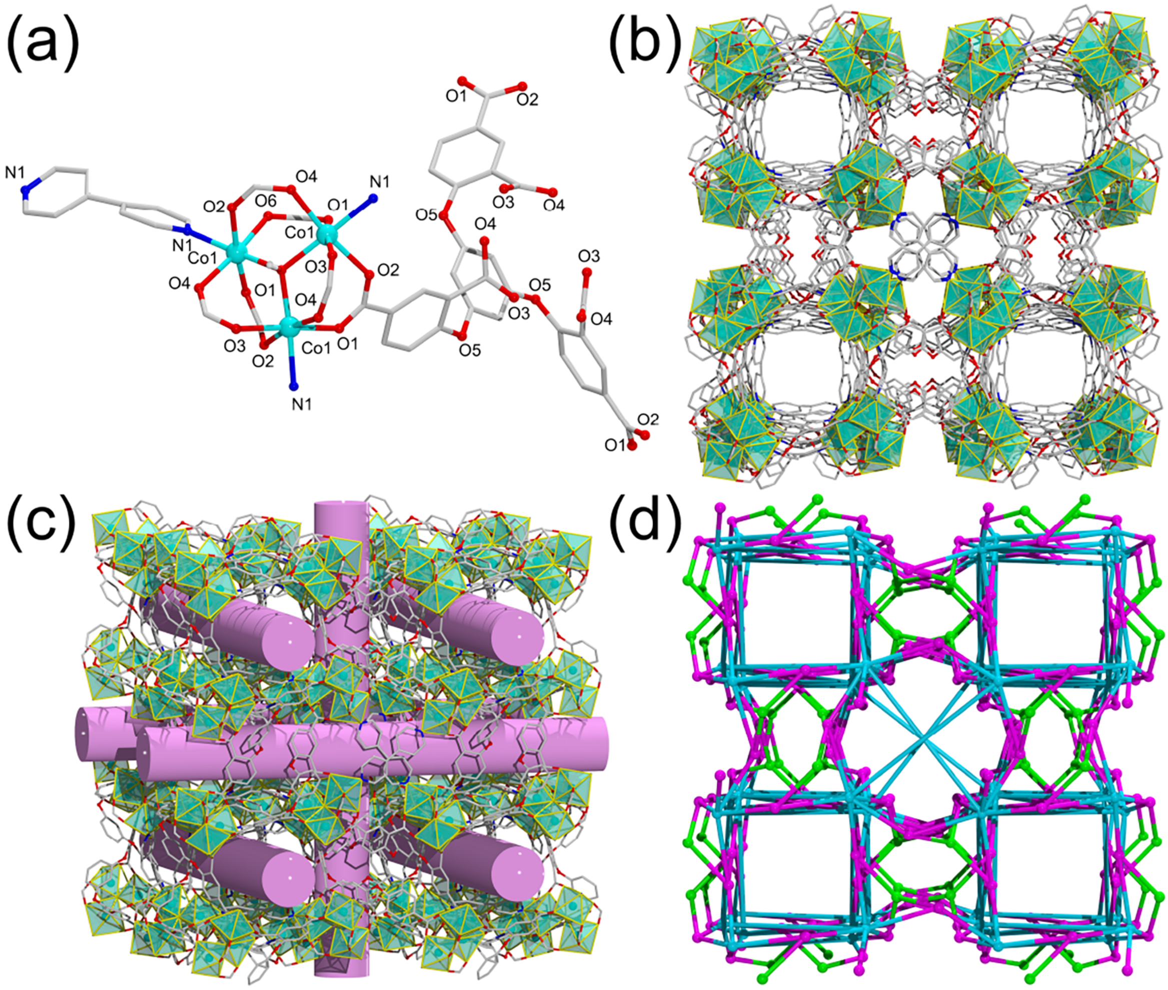

Figure 1. (a) Trinuclear cluster of $[Co_3(COO)_6N_3(\mu_3\text{-}OH)]$; (b) 1D square tubular channels viewed along the *a* axis; (c) 3D porous framework; (d) topology of **1**.

adsorbents for C_2H_6-selectivity need to contain rich nonpolar/inert surfaces, such as aromatic moieties, which facilitates the capture of gas molecules with high polarizability.[34−41]

Along this line, we built a saturated trinuclear metal cluster $[Co_3(COO)_6N_3(\mu_3\text{-}OH)]$ to construct MOFs, which can diminish the affinity for C_2H_4 and C_2H_2, and a combination of a flexible ligand enriched with aromatic rings (4,4′,4″-(benzene-1,3,5-triyltris(oxy))triisophthalic acid = H_6tipa) as well as 4,4′-bipyridine (bpy), an ultramicroporous MOF $[Co_3(\mu_3\text{-}OH)(tipa)(bpy)_{1.5}]\cdot 3DMF\cdot 6H_2O$ (**1**) with standalone one-dimensional (1D) square tubular channels that was successfully constructed. The MOF features nonpolar/inert pore surfaces enriched with plenty of aromatic rings, and the activation of **1** shows preferential adsorption of C_2H_6 compared to C_2H_4 and C_2H_2 in the low-pressure region, which is further verified by adsorption heats and selectivities. Moreover, transient breakthrough simulations suggest that the MOF can purify C_2H_4 from binary C_2H_6/C_2H_4 (50/50 and 10/90) and ternary $C_2H_4/C_2H_6/C_2H_2$ (89/10/1). The deep mechanism of C_2H_4 separation was studied by GCMC simulations.

2. EXPERIMENTAL SECTION

2.1. Materials and Methods. All reagents were obtained directly from suppliers and used without further purification. Powder X-ray diffraction (PXRD) data at room temperature were collected on an X-ray powder diffractometer (Bruker D8 ADVANCE) with a scan rate of 5.0° per minute in an air atmosphere. Thermogravimetric analysis (TGA) was carried out on a NETZSCH TG 209 thermal analyzer, which was heated at a rate of 10 °C min^{-1} from 30 to 800 °C and with a nitrogen condition. A Nicolet FTIR 170 SX spectrophotometer was used to record the Fourier transform infrared spectrum (FTIR). Elemental analyses were conducted on a PerkinElmer 2400C elemental analyzer. Gas and water vapor sorption measurements were performed using property testing and analyzed using a Quantachrome Autosorb-iQ MP apparatus.

2.2. Synthesis of $[Co_3(\mu_3\text{-}OH)(tipa)(bpy)_{1.5}]\cdot 3DMF\cdot 6H_2O$ (1). $Co(NO_3)_2\cdot 6H_2O$ (10.1 mg, 0.05 mmol), H_6tipa (12.3 mg, 0.02 mmol), and bpy (3.2 mg, 0.02 mmol) were added to a mixture of 2.5 mL of DMF and 0.5 mL of deionized water. Then, the mixture was mixed into a Teflon-lined stainless steel (25 mL) container and heated at 120 °C for 72 h. After reducing to room temperature at a speed of 10 °C h^{-1}, the purple-red cube-shaped crystals were obtained in 49.5% yield. Anal. calcd. (%) for C_{54} H_{58} Co_3 N_6 O_{25}: C, 47.42; H, 4.27; N, 6.14. Found: C, 47.51; H, 4.31; N, 6.12. IR data (KBr, cm^{-1}): 3423(m), 2966(w), 2937(w), 2807(w), 2722(w), 1631(s), 1595(s), 1385(m), 1350(m), 1277(w), 1116(m), 982(w), 764(m), 682(w), 619(m), 516(w).

2.3. X-ray Crystallography. A Bruker SMART APEX II CCD detector was employed to calculate the single-crystal X-ray diffraction data of **1** with Cu-Kα radiation (λ = 1.54184 Å) at 170 K. The structure of **1** was solved by the direct methods and refined by the full-matrix least-squares methods based on F^2 by the SHELXTL[42] software package. The non-hydrogen atoms of the framework were

https://doi.org/10.1021/acsami.3c04225
ACS Appl. Mater. Interfaces 2023, 15, 23538−23545

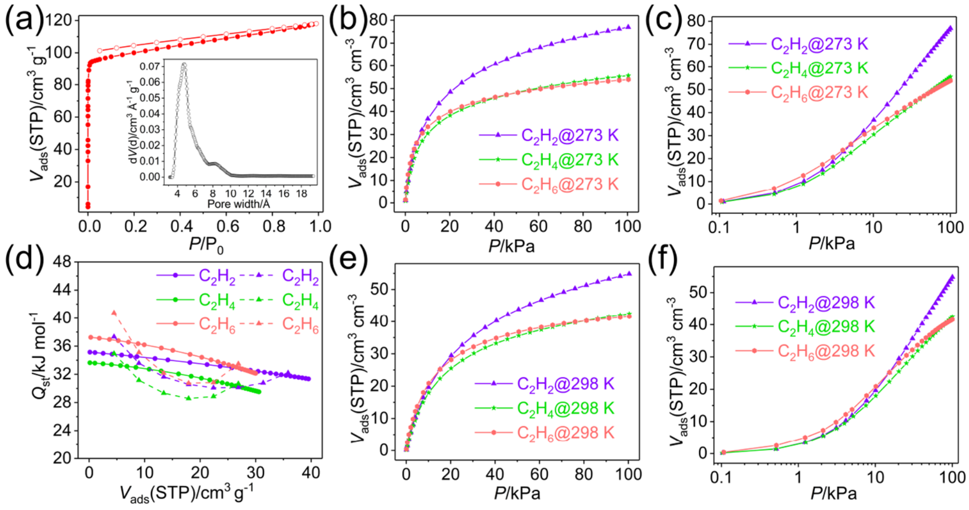

Figure 2. (a) N_2 adsorption isotherm at 77 K, inset: porous size distribution; gas sorption isotherms for C_2 hydrocarbons at (b, c) 273 K and (e, f) 298 K; (d) adsorption heats of **1a** calculated using virial (solid lines) and Clausius−Clapeyron (dotted lines) methods.

refined anisotropically, whereas all the hydrogen atoms were geometrically located and were refined isotropically. As the solvent molecules of the data in **1** cannot be located, the SQUEEZE routine of PLATON[43] was applied in refining. The selected crystallographic data are summarized in Table S2, and the CCDC number for **1** is 2233223.

3. RESULTS AND DISCUSSION

3.1. Crystal Structure of 1. Single-crystal X-ray diffraction analysis reveals that **1** crystallizes in the trigonal system with the $P\bar{4}3n$ space group featuring 1D square tubular channels. The asymmetric unit consists of one Co(II) ion, one-third of the tipa ligand, one-half of the bpy ligand, and a third of μ_3-OH. Each Co(II) is located in a slightly distorted octahedral geometry, linked by one μ_3-OH oxygen atom, four carboxylic oxygen atoms (Co1-O = 2.0528(18) to 2.137(7) Å) from three different tipa ligands, and a nitrogen atom (Co1-N = 2.154(8) Å) from one bpy ligand (Table S3 and Figure S1a). The adjacent Co1 atoms are further bridged *via* μ_3-OH and deprotonated carboxylate possessing the same μ_2-η^1:η^1 coordination modes to generate a trinuclear cluster SBU of $[Co_3(COO)_6N_3(\mu_3\text{-}OH)]$ (Figure 1a and Figure S1b). Moreover, the trinuclear cluster joint ligand results in a 3D porous framework with stand-alone 1D square tubular channels along the *a*, *b*, and *c* axis (Figure 1b,c), which have ultramicropore sizes of 4.8 Å and a porosity of 28.7% calculated by PLATON[43] using the contact surface and a probe radius of 1.2 Å. Importantly, these 1D square tubular channels are enriched with plenty of aromatic rings causing nonpolar/inert pore surfaces, which would be in favor of adsorbing higher polarizability of gas molecules. From the topological perspective, the trinuclear cluster of $[Co_3(COO)_6N_3(\mu_3\text{-}OH)]$ can be viewed as a 9-connected node, and the benzene ring in the middle of the ligand and carboxyl benzene of the ligand both can be regarded as 3-connected nodes. Thus, the whole framework exhibits a trinodal (3,3,9)-connected network with the point symbol of $(4.5.7)_3(4^3.5^9.6^6.7^{15}.8^3)(4^3)$ (Figure 1d).

3.2. PXRD and TGA. The experimental PXRD pattern of **1** is in excellent agreement with the simulated pattern obtained from the single-crystal X-ray diffraction data, revealing the phase purity (Figure S3). Additionally, PXRD of samples exposed to air for half a year is consistent with the simulated pattern, which indicates that **1** has good stability in air (Figure S3). TGA shows a weight loss of about 6.9% caused by the loss of the six free water molecules (calcd. 6.7%) before 115 °C. Then, a weight loss of 13.0% from 115 to 260 °C corresponds to the loss of three guest DMF molecules (calcd. 13.7%). Further heating to 340 °C induced structural decomposition (Figure S4).

3.3. Sorption and Separation Performances. Before evaluating the porosity of **1**, the CH_2Cl_2-exchanged samples were heated at 120 °C for 8 h under vacuum to remove the free solvent molecules, and PXRD and TGA denote the stability of the activated samples and removal of guest molecules. Moreover, the color of the samples changed from light red to dark purple during the solvent removal process, which may be because removal of polar solvents leads to the transfer of electrons in the ligand so as to absorb or radiate a certain wavelength of light (Figure S5). The N_2 sorption isotherm at 77 K is measured to confirm the permanent porosity of **1a** (Figure 2a). The type-I isotherm adsorption behavior of ultramicroporous materials with a saturation uptake of 118.1 cm^3 g^{-1} is revealed. However, the N_2 adsorption isotherm at 77 K does not show a plateau, which may be because large pores are formed by accumulation between crystal particles, causing nitrogen to be adsorbed all the time, and the phenomenon does not affect the values of surface areas and pore size distribution. The Brunauer−Emmett−Teller (BET) and Langmuir surface areas of **1a** are measured to be 408.4 and 446.8 m^2 g^{-1}, respectively. The pore size distribution is around 4.8 Å calculated by the Horvath−Kawazoe method, coinciding with the sizes of the aperture. A pore volume of 0.183 cm^3 g^{-1} assessed at $P/P_0 \approx 0.99$ is almost equal to the value of 0.207 cm^3 g^{-1} obtained from the crystal structure. In addition, the hydrophobic character of the pore surface of **1a** that covers abundant aromatic π-systems was verified by the type-V water sorption isotherm tested at 298 K (Figure S6).[44]

The nonpolar/inert pore surface and narrow pore size inspired us to research gas adsorption performance of the C_2 hydrocarbons. To ensure accuracy of the data, the adsorption isotherms of **1a** for C_2H_6, C_2H_4, and C_2H_2 were recorded three times at 273, 288, and 298 K, respectively, and isotherms with

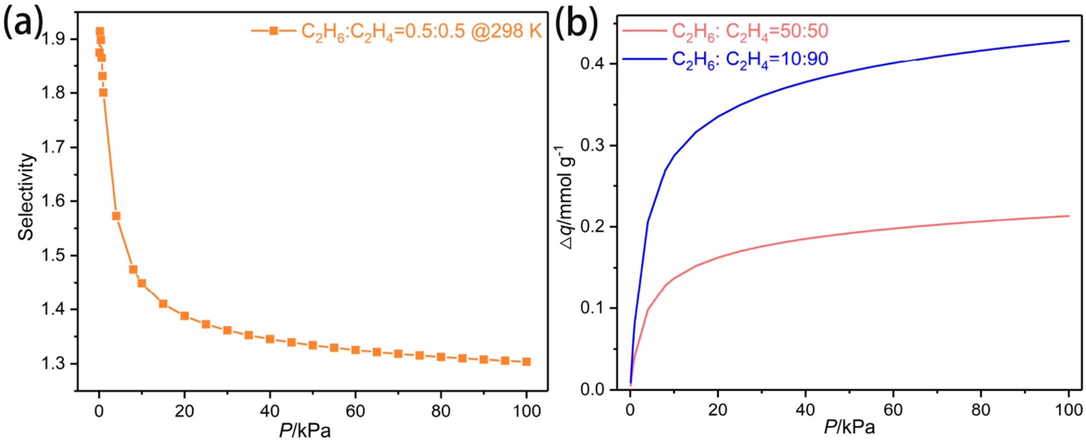

Figure 3. (a) Selectivities of the equimolar C_2H_6/C_2H_4 mixture; (b) separation potential for 50/50 and 10/90 mixtures of C_2H_6/C_2H_4.

error bars are shown in Figures S8 and S9. To clearly compare the adsorption performance in the low pressure, Figure 2c,f and Figure S7b are drawn on the log scale. Under 100 kPa, **1a** shows the highest C_2H_2 loadings (77.0 and 54.8 $cm^3\ cm^{-3}$) compared with C_2H_6 (54.0 and 41.6 $cm^3\ cm^{-3}$) and C_2H_4 (55.7 and 42.4 $cm^3\ cm^{-3}$) at 273 and 298 K (Figure 2b,c,e,f), respectively, due to the critical temperature of C_2H_2 (35.15 °C), higher than those of C_2H_6 (32.25 °C) and C_2H_4 (9.45 °C). However, the gas adsorption amount of C_2H_6 is higher than those of C_2H_4 and C_2H_2 in the low-pressure location (below 15.3 kPa at 298 K and 5.1 kPa at 273 K). Furthermore, the C_2H_6 adsorption isotherm presents a steeper curve than those of C_2H_4 and C_2H_2 in the low-pressure region at different temperatures, indicating the stronger binding between C_2H_6 and the framework. The result shows that **1a** is the preferential adsorption for C_2H_6 compared to C_2H_4 and C_2H_2, and the peculiar reversed adsorption phenomenon is different from the vast majority of reported MOFs. This rare phenomenon broke the traditional understanding of the relationship between C_2 hydrocarbons.

In addition, the C_2H_6 and C_2H_4 adsorption uptake values at 100 kPa are higher than those of some reported famous MOFs, such as NUM-3a (298 K: 20.4 $cm^3\ cm^{-3}$ for C_2H_6 and 28.9 $cm^3\ cm^{-3}$ for C_2H_4; 273 K: 23.0 $cm^3\ cm^{-3}$ for C_2H_6 and 34.9 $cm^3\ cm^{-3}$ for C_2H_4),[45] BSF-2 (34.1 $cm^3\ cm^{-3}$ for C_2H_6 at 298 K),[46] and UPC-33 (32.7 $cm^3\ cm^{-3}$ for C_2H_6 at 298 K),[47] but these are still lower than those of iso-MOF-4 (71.6 $cm^3\ cm^{-3}$ for C_2H_6 at 298 K),[48] Azole-Th-1 (298 K: 132.5 $cm^3\ cm^{-3}$ for C_2H_6 and 106.7 $cm^3\ cm^{-3}$ for C_2H_4),[49] and NIIC-20-Pr (88.3 $cm^3\ cm^{-3}$ for C_2H_4 at 273 K).[50] Meanwhile, the adsorption capacity of C_2H_2 at 298 K is lower than ZNU-6 (193.8 $cm^3\ cm^{-3}$)[51] but far higher than those of JLU-Liu33F (14.5 $cm^3\ cm^{-3}$)[52] and UPC-71 (25.1 $cm^3\ cm^{-3}$).[53]

To further understand the unique reverse adsorption phenomenon, the gas affinities toward C_2 hydrocarbons are estimated with the adsorption heat (Q_{st}) value calculated from single-component isotherms at 273, 288, and 298 K by utilizing the virial equation. The sequence of the Q_{st} values is C_2H_6 (37.2 kJ mol^{-1}) > C_2H_2 (35.1 kJ mol^{-1}) > C_2H_4 (33.6 kJ mol^{-1}) at zero loading (Figure 2d), which is consistent with uptake values at the low-pressure region and the steepness of the isotherms because the Q_{st} value at zero loading is the most energetically favored site in the framework interacting with gas molecules. The Q_{st} of C_2H_6 are higher than those of C_2H_2 and C_2H_4 below a loading of 27.6 $cm^3\ g^{-1}$, suggesting the small pore size and aromatic rings in **1a** that lead to a stronger C_2H_6 binding affinity. Then, the Q_{st} value for C_2H_6 is still greater than that for C_2H_4 with the increase in gas loadings, and the final order of Q_{st} values is C_2H_2 > C_2H_6 > C_2H_4. Notably, the Q_{st} value of C_2H_6 at zero loading is higher than those of famous MOFs, such as CAU-11 (31.0 kJ mol^{-1}),[54] BUT-315-a (33.4 kJ mol^{-1}),[55] JXNU-9 (23.6 kJ mol^{-1}),[56] and $Fe_2(BDP)_3$ (23.9 kJ mol^{-1})[57] and lower than those of MAF-49 (60 kJ mol^{-1})[58] and NKMOF-8-Br (40.8 kJ mol^{-1}).[59] In addition, the Clausius−Clapeyron equation was also used to obtain the isosteric heat of adsorption. The Q_{st} of C_2H_6, C_2H_4, and C_2H_2 lie in the ranges of 40.8−30.8, 37.3−30.1, and 34.9−28.6 kJ mol^{-1}, respectively, which show a similar trend with those acquired from the virial equation (Figure 2d).

The ideal adsorbed solution theory (IAST) was employed to calculate the selectivity for C_2H_6/C_2H_4 mixtures at 298 K. Derived by Myers and Prausnitz,[60] the IAST is a method for predicting the adsorption equilibria for components in a mixture, using only single-component adsorption data at the same temperature and on the same adsorbent. IAST is based on three assumptions: (i) the same surface area is available to all adsorbates, (ii) the adsorbent is inert, and (iii) the multicomponent mixture behaves as an ideal solution at constant spreading pressure and temperature. The selectivity for equimolar C_2H_6/C_2H_4 mixtures is 1.30 at 298 K and 100 kPa (Figure 3a). Although this C_2H_6/C_2H_4 selectivity at 298 K is lower than some famous MOFs, such as BUT-315-a (2.35),[55] MIL-142A (1.5),[61] and Zn-FBA (2.9),[62] it is comparable to Zn-atz-oba (1.27)[63] and LIFM-28 (1.24).[64] In addition, the separation potential ($\Delta q = q_1 y_2/y_1 - q_2$) is utilized to further assess C_2H_6/C_2H_4 separation performance, which as a comprehensive index integrating adsorption capacity and selectivity is proposed by Krishna first[65] and provides a convenient and simple indicator for the separation ability of MOFs based on IAST. The Δq values for 50/50 and 10/90 mixtures of C_2H_6/C_2H_4 are 0.18 and 0.38 mmol g^{-1} at 298 K and 100 kPa (Figure 3b), respectively. These results reflect that **1a** could efficiently separate C_2H_4 from the C_2H_6/C_2H_4 mixture at an ambient environment.

3.4. Breakthrough Simulations. To further confirm the C_2H_4 separation performance of **1a** for industrial components, the transient breakthrough simulations for 50/50 and 10/90 mixtures of C_2H_6/C_2H_4 as well as 89/10/1 mixtures of $C_2H_4/C_2H_6/C_2H_2$ were conducted at 298 K. The simulation methodology is described in earlier works,[66,67] and details

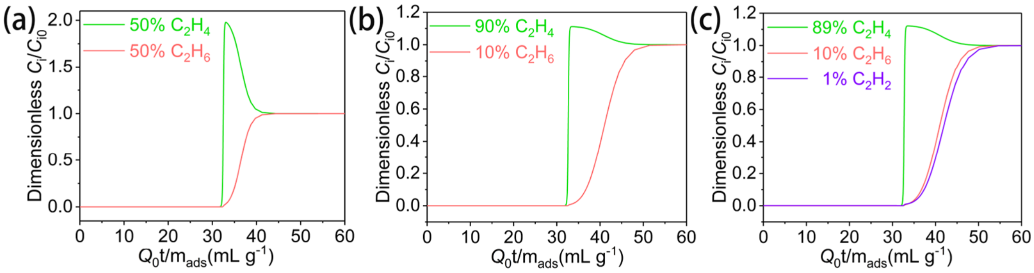

Figure 4. Simulated breakthrough curves for (a) 50/50 and (b) 10/90 mixtures of C_2H_6/C_2H_4; (c) 89/10/1 mixtures of $C_2H_4/C_2H_6/C_2H_2$ at 298 K and 100 kPa.

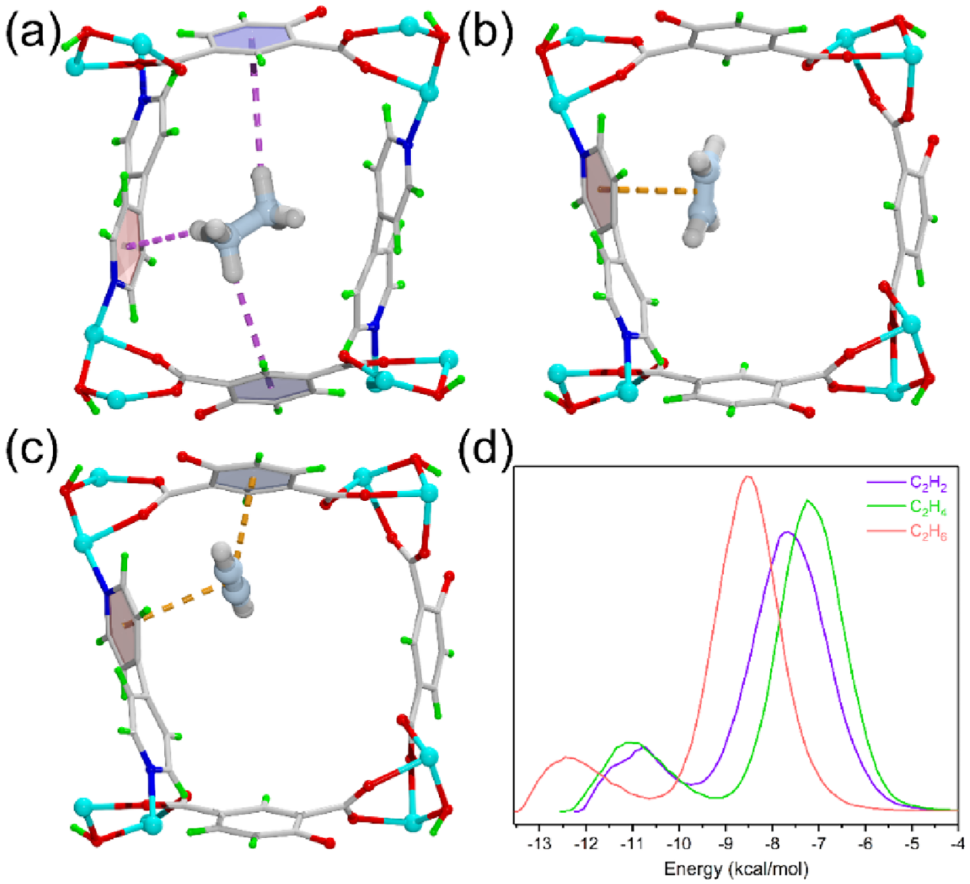

Figure 5. Binding sites between **1a** and (a) C_2H_6, (b) C_2H_4, and (c) C_2H_2; (d) energy distribution curves of C_2H_2, C_2H_4, and C_2H_6.

are provided in the Supporting Information. For 50/50 and 10/90 mixtures of C_2H_6/C_2H_4, C_2H_4 first appeared at the outlet of the column, while C_2H_6 breakthrough occurred after calculations of 32.4 and 32.9 mL g^{-1}, respectively (Figure 4a,b). Moreover, 89/10/1 mixtures of $C_2H_4/C_2H_6/C_2H_2$ pass through the bed with the sequence of C_2H_4, C_2H_2, and C_2H_6 (Figure 4c), indicating that C_2H_4 can also be effectively separated from $C_2H_4/C_2H_6/C_2H_2$ mixtures.

3.5. Molecular Simulations. To gain an insight into the unique reversed adsorption mechanism, grand canonical Monte Carlo (GCMC) simulations were performed to research binding sites of C_2 hydrocarbons in **1a** at 298 K and 5 kPa. The C_2H_6 molecule is almost located in the center of the pore and connects with two opposite benzene ring stems from two tipa ligands and one pyridine ring from the bpy ligand through three $C-H_{C2H6}\cdots\pi_{\text{aromatic rings}}$ interactions ($H_{C2H6}\cdots\pi_{\text{aromatic rings}}$ = 2.71−4.22 Å) (Figure 5a), which are less than/comparable with the sum of the van der Waals radii of hydrogen (1.20 Å) and carbon (1.70 Å) atoms, demonstrating strong attractive interactions. Different from the C_2H_6 molecule, the C_2H_4 and C_2H_2 molecules locate at the corner of the channel and interact with the pyridine ring from bpy ligands to generate weak $\pi_{C2H4/C2H2}\cdots\pi_{bpy}$ interactions ($\pi_{C2H4/C2H2}\cdots\pi_{bpy}$ = 3.68−3.72 Å) through π-electrons in the unsaturated carbon−carbon bonds of guests (Figure 5b,c). For C_2H_2, there is also a $\pi_{C2H2}\cdots\pi_{tipa}$ interaction ($\pi_{C2H2}\cdots\pi_{tipa}$ = 3.51 Å) formed by the C_2H_2 molecule with one benzene ring (Figure 5c). As a result, the shortest and most number of C−H⋯π interactions between C_2H_6 and the framework coincide with the steepest adsorption isotherms and the highest Q_{st} value of C_2H_6. Interestingly, it is found that adjacent C_2H_2 in channels form intermolecular interactions with each other by $H_{C2H2}\cdots\pi_{C2H2}$ contacts (2.75−3.00 Å) at 298 K and 100 kPa (Figure S14), indicating that the narrow channels enhance the potential fields for C_2H_2 molecules and result in C_2H_2 packing, coinciding with the highest C_2H_2 adsorption amount under high pressure.

In addition, the particular reversed adsorption phenomenon can be further supported by the energy distribution curves of **1a**. The order of energy values (C_2H_6 (8.55 kcal/mol) > C_2H_2 (7.65 kcal/mol) > C_2H_4 (7.25 kcal/mol)) is in line with Q_{st} values (Figure 5d).

4. CONCLUSIONS

In summary, a nonpolar/inert MOF with an ultramicroporous aperture decorated with plenty of aromatic rings was successfully prepared, which realizes highly reversed separation of C_2H_4 from C_2 hydrocarbons. The particular pore environment and suitable pore aperture of **1a** lead to a stronger interaction for C_2H_6 than those of C_2H_4 and C_2H_2, which can be well supported by adsorption heat, C_2H_6/C_2H_4 selectivity, favorable breakthrough simulations, and molecular simulation. This contribution will facilitate the design and construction of nonpolar/inert MOFs for challenging C_2H_4 separation from C_2 hydrocarbon mixtures.

■ ASSOCIATED CONTENT

Supporting Information

The Supporting Information is available free of charge at https://pubs.acs.org/doi/10.1021/acsami.3c04225.

> The crystallographic data; selected bond lengths and bond angles; PXRD pattern; TGA curves; water vapor adsorption isotherm; cyclic gas sorption isotherms; calculation of sorption heat; gas selectivity prediction *via* IAST; transient breakthrough simulations; GCMC simulation methodology (PDF)

■ AUTHOR INFORMATION

Corresponding Authors

Xiu-Yuan Li − *Shaanxi Key Laboratory of Optoelectronic Functional Materials and Devices, School of Materials Science and Chemical Engineering, Xi'an Technological University, Xi'an 710021, P. R. China*; orcid.org/0000-0002-3508-9864; Email: lixiuyuan@xatu.edu.cn

Chaozheng He − *Shaanxi Key Laboratory of Optoelectronic Functional Materials and Devices, School of Materials Science and Chemical Engineering, Xi'an Technological University, Xi'an 710021, P. R. China*; Email: hecz2019@xatu.edu.cn

Authors

Hai-Yu Duan − *Shaanxi Key Laboratory of Optoelectronic Functional Materials and Devices, School of Materials Science and Chemical Engineering, Xi'an Technological University, Xi'an 710021, P. R. China*

Rajamani Krishna − *Van't Hoff Institute for Molecular Sciences, University of Amsterdam, 1098 XH Amsterdam, The Netherlands*; orcid.org/0000-0002-4784-8530

Complete contact information is available at:
https://pubs.acs.org/10.1021/acsami.3c04225

Author Contributions

H.-Y.D.: Writing−original draft and data curation. X.-Y.L.: Writing−review and editing, funding acquisition, conceptualization, and supervision. R.K.: Methodology and data curation. C.H.: Funding acquisition.

Notes

The authors declare no competing financial interest.

■ ACKNOWLEDGMENTS

This work is supported by the Young Talent fund of University Association for Science and Technology in Shaanxi, China (20200608), NSF of Shaanxi Province (2021JQ-642), and NSF of the Education Department of Shaanxi Province (21JK0687).

■ REFERENCES

(1) Zhang, Z.; Peh, S. B.; Wang, Y.; Kang, C.; Fan, W.; Zhao, D. Efficient Trapping of Trace Acetylene from Ethylene in an Ultramicroporous Metal−Organic Framework: Synergistic Effect of High-Density Open Metal and Electronegative Sites. *Angew. Chem., Int. Ed.* **2020**, *59*, 18927−18932.

(2) Pires, J.; Fernandes, J.; Dedecker, K.; Gomes, J. R. B.; Pérez-Sánchez, G.; Nouar, F.; Serre, C.; Pinto, M. L. Enhancement of Ethane Selectivity in Ethane−Ethylene Mixtures by Perfluoro Groups in Zr-Based Metal-Organic Frameworks. *ACS Appl. Mater. Interfaces* **2019**, *11*, 27410−27421.

(3) Tang, H.; Jiang, J. In Silico Screening and Design Strategies of Ethane-Selective Metal−Organic Frameworks for Ethane/Ethylene Separation. *AIChE J.* **2020**, *67*, No. e17025.

(4) Zhang, P.-D.; Zhang, X.; Wu, X.-Q.; Xu, Z.-C.; Li, J.-R. Boosting C_2H_6/C_2H_4 Separation in Scalable Metal-Organic Frameworks through Pore Engineering. *AIChE J.* **2022**, *68*, No. e17752.

(5) Wang, R.; Gao, Q.; Zhong, Y.; Wang, X.; Xu, D. Molecular Insights into the Role of O_2 in Reversed C_2H_6/C_2H_4 Separation on Metal−Organic Frameworks. *Sep. Purif. Technol.* **2022**, *304*, No. 122332.

(6) Li, Y.-P.; Fan, S.-C.; Zhang, G.-T.; Zhai, Q.-G. Pore-Window Partitions in Metal−Organic Frameworks for Highly Efficient Reversed Ethylene/Ethane Separations. *Inorg. Chem.* **2022**, *61*, 10493−10501.

(7) Gu, X.-W.; Pei, J.; Shao, K.; Wen, H.-M.; Li, B.; Qian, G. Chemically Stable Hafnium-Based Metal−Organic Framework for Highly Efficient C_2H_6/C_2H_4 Separation under Humid Conditions. *ACS Appl. Mater. Interfaces* **2021**, *13*, 18792−18799.

(8) Chen, D.-M.; Sun, C.-X.; Zhang, N.-N.; Si, H.-H.; Liu, C.-S.; Du, M. Tunable Robust Pacs-mofs: a Platform for Systematic Enhancement of the C_2H_2 Uptake and C_2H_2/C_2H_4 Separation Performance. *Inorg. Chem.* **2018**, *57*, 2883−2889.

(9) Chen, K.-J.; Madden, D. G.; Mukherjee, S.; Pham, T.; Forrest, K. A.; Kumar, A.; Space, B.; Kong, J.; Zhang, Q.-Y.; Zaworotko, M. J. Synergistic Sorbent Separation for One-Step Ethylene Purification from a four-Component Mixture. *Science* **2019**, *366*, 241−246.

(10) Lv, D.; Shi, R.; Chen, Y.; Wu, Y.; Wu, H.; Xi, H.; Xia, Q.; Li, Z. Selective Adsorption of Ethane over Ethylene in PCN-245: Impacts of Interpenetrated Adsorbent. *ACS Appl. Mater. Interfaces* **2018**, *10*, 8366−8373.

(11) Lin, R.-B.; Li, L.; Zhou, H.-L.; Wu, H.; He, C.; Li, S.; Krishna, R.; Li, J.; Zhou, W.; Chen, B. Molecular Sieving of Ethylene from Ethane using a Rigid Metal−Organic Framework. *Nat. Mater.* **2018**, *17*, 1128−1133.

(12) Wang, S.-M.; Wang, F.; Dong, Y.-L.; Shivanna, M.; Dong, Q.; Mu, X.-T.; Duan, J.; Yang, Q.; Zaworotko, M. J.; Yang, Q.-Y. Reversed C_2H_6/C_2H_4 Separation in Interpenetrated Diamondoid Coordination Networks with Enhanced Host−Guest Interaction. *Sep. Purif. Technol.* **2021**, *276*, No. 119385.

(13) Zeng, H.; Xie, X.-J.; Xie, M.; Huang, Y.-L.; Luo, D.; Wang, T.; Zhao, Y.; Lu, W.; Li, D. A Cage-Interconnected Metal-Organic Framework with Tailored Apertures for Efficient C_2H_6/C_2H_4 Separation under Humid Conditions. *J. Am. Chem. Soc.* **2019**, *141*, 20390−20396.

(14) Jiang, Y.; Jia, S.; Liu, X.-Q.; Cui, P.; Sun, L.-B. Selective Adsorption of Ethane over Ethylene through a Metal−Organic

Framework Bearing Dense Alkyl Groups. *Sep. Purif. Technol.* **2022**, *295*, No. 121330.

(15) Lou, W.; Li, J.; Sun, W.; Hu, Y.; Wang, L.; Neumann, R. F.; Steiner, M.; Gu, Z.; Luan, B.; Zhang, Y. Screening Hoffman-Type Metal Organic Frameworks for Efficient C_2H_2/CO_2 Separation. *Chem. Eng. J.* **2023**, *452*, No. 139296.

(16) Mu, X.-T.; Ouyang, Y.-S.; Pei, L.-M.; Peng, Z.-X.; Shao, S.-Q.; Wang, S.-M.; Xiong, H.; Xiao, Y.; Yang, Q.-Y. Control of Pore Environment in Highly Porous Carbon Materials for C_2H_6/C_2H_4 Separation with Exceptional Ethane Uptake. *Mater. Today Chem.* **2022**, *24*, No. 100856.

(17) Zeng, H.; Xie, M.; Wang, T.; Wei, R.-J.; Xie, X.-J.; Zhao, Y.; Lu, W.; Li, D. Orthogonal-Array Dynamic Molecular Sieving of Propylene/Propane Mixtures. *Nature* **2021**, *595*, 542−548.

(18) Li, J.; Bhatt, P. M.; Li, J.; Eddaoudi, M.; Liu, Y. Recent Progress on Microfine Design of Metal-Organic Frameworks: Structure Regulation and Gas Sorption and Separation. *Adv. Mater.* **2020**, *32*, 2002563.

(19) Xie, X.; Zeng, H.; Xie, M.; Chen, W.; Hua, G.; Lu, W.; Li, D. A Metal-Organic Framework for C_2H_2/CO_2 Separation under Highly Humid Conditions: Balanced Hydrophilicity/Hydrophobicity. *Chem. Eng. J.* **2021**, *427*, No. 132033.

(20) Wang, D.; Zhang, J.; Li, G.; Yuan, J.; Li, J.; Huo, Q.; Liu, Y. Mesoporous Hexanuclear Copper Cluster-Based Metal−Organic Framework with Highly Selective Adsorption of Gas and Organic Dye Molecules. *ACS Appl. Mater. Interfaces* **2018**, *10*, 31233−31239.

(21) Peng, Y.-L.; Pham, T.; Li, P.; Wang, T.; Chen, Y.; Chen, K.-J.; Forrest, K. A.; Space, B.; Cheng, P.; Zaworotko, M. J.; Zhang, Z. Robust Ultramicroporous Metal−Organic Frameworks with Benchmark Affinity for Acetylene. *Angew. Chem., Int. Ed.* **2018**, *57*, 10971−10975.

(22) Zhou, P.; Yue, L.; Wang, X.; Fan, L.; Chen, D.-L.; He, Y. Improving Ethane/Ethylene Separation Performance of Isoreticular Metal−Organic Frameworks via Substituent Engineering. *ACS Appl. Mater. Interfaces* **2021**, *13*, 54059−54068.

(23) Li, X.-Y.; Duan, H.-Y.; He, C. Engineering a Series of Isoreticular Pillared Layer Ultramicroporous MOFs for Gas and Vapor Uptake. *Inorg. Chem.* **2022**, *61*, 17634−17640.

(24) Jiang, Y.; Hu, J.; Wang, L.; Sun, W.; Xu, N.; Krishna, R.; Duttwyler, S.; Cui, X.; Xing, H.; Zhang, Y. Comprehensive Pore Tuning in an Ultrastable Fluorinated Anion Cross-Linked Cage-like MOF for Simultaneous Benchmark Propyne Recovery and Propylene Purification. *Angew. Chem., Int. Ed.* **2022**, *61*, No. e20220094.

(25) Gao, D.; Ding, T.; Yan, W.-W.; Zheng, L.-N.; Xie, K.-F.; Gao, Z.-W. Two Structurally Similar Co_5 Cluster-Based Metal−Organic Frameworks Containing Open Metal Sites for Efficient C_2H_2/CO_2 Separation. *Inorg. Chem.* **2022**, *61*, 20026−20034.

(26) Wang, H.-T.; Chen, Q.; Zhang, X.; Zhao, Y.-L.; Xu, M.-M.; Lin, R.-B.; Huang, H.; Xie, L.-H.; Li, J.-R. Two Isostructural Metal−Organic Frameworks with Unique Nickel Clusters for $C_2H_2/C_2H_6/C_2H_4$ Mixture Separation. *J. Mater. Chem. A* **2022**, *10*, 12497−12502.

(27) Li, Y.; Zhang, X.; Lan, J.; Xu, P.; Sun, J. Porous Zn(Bmic)(AT) MOF with Abundant Amino Groups and Open Metal Sites for Efficient Capture and Transformation of CO_2. *Inorg. Chem.* **2019**, *58*, 13917−13926.

(28) Dong, H.; Zhang, X.; Lu, Y.; Yang, Y.; Zhang, Y.-P.; Tang, H.-L.; Zhang, F.-M.; Yang, Z.-D.; Sun, X.; Feng, Y. Regulation of Metal Ions in Smart Metal-Cluster Nodes of Metal-Organic Frameworks with Open Metal Sites for Improved Photocatalytic CO_2 Reduction Reaction. *Appl. Catal., B* **2020**, *276*, No. 119173.

(29) Gu, X.-W.; Wang, J.-X.; Wu, E.; Wu, H.; Zhou, W.; Qian, G.; Chen, B.; Li, B. Immobilization of Lewis Basic Sites into a Stable Ethane-Selective MOF Enabling One-Step Separation of Ethylene from a Ternary Mixture. *J. Am. Chem. Soc.* **2022**, *144*, 2614−2623.

(30) Wang, G.-D.; Li, Y.-Z.; Shi, W.-J.; Hou, L.; Wang, Y.-Y.; Zhu, Z. One-Step C_2H_4 Purification from Ternary $C_2H_6/C_2H_4/C_2H_2$ Mixtures by a Robust Metal-Organic Framework with Customized Pore Environment. *Angew. Chem., Int. Ed.* **2022**, *61*, No. e202205427.

(31) Li, Y.; Xie, Y.; Zhang, X.; Velasco, E.; Chen, Q.; Li, J.-R. Enhancing Ethane/Ethylene Separation Performance in Two Dynamic MOFs by Regulating Temperature-Controlled Structural Interpenetration. *Inorg. Chem.* **2022**, *62*, 4762−4769.

(32) Zhu, B.; Cao, J.-W.; Mukherjee, S.; Pham, T.; Zhang, T.; Wang, T.; Jiang, X.; Forrest, K. A.; Zaworotko, M. J.; Chen, K.-J. Pore Engineering for One-Step Ethylene Purification from a Three-Component Hydrocarbon Mixture. *J. Am. Chem. Soc.* **2021**, *143*, 1485−1492.

(33) Di, Z.; Liu, C.; Pang, J.; Zou, S.; Ji, Z.; Hu, F.; Chen, C.; Yuan, D.; Hong, M.; Wu, M. A Metal-Organic Framework with Nonpolar Pore Surfaces for the One-Step Acquisition of C_2H_4 from a C_2H_4 and C_2H_6 Mixture. *Angew. Chem., Int. Ed.* **2022**, *61*, No. e202210343.

(34) Kang, M.; Kang, D. W.; Choe, J. H.; Kim, H.; Kim, D. W.; Park, H.; Hong, C. S. A Robust Hydrogen-Bonded Metal−Organic Framework with Enhanced Ethane Uptake and Selectivity. *Chem. Mater.* **2021**, *33*, 6193−6199.

(35) Hao, H. G.; Zhao, Y. F.; Chen, D. M.; Yu, J. M.; Tan, K.; Ma, S.; Chabal, Y.; Zhang, Z. M.; Dou, J. M.; Xiao, Z. H.; Day, G.; Zhou, H. C.; Lu, T. B. Simultaneous Trapping of C_2H_2 and C_2H_6 from a Ternary Mixture of $C_2H_2/C_2H_4/C_2H_6$ in a Robust Metal−Organic Framework for the Purification of C_2H_4. *Angew. Chem., Int. Ed.* **2018**, *57*, 16067−16071.

(36) Pei, J.; Wang, J.-X.; Shao, K.; Yang, Y.; Cui, Y.; Wu, H.; Zhou, W.; Li, B.; Qian, G. Engineering Microporous Ethane-Trapping Metal−Organic Frameworks for Boosting Ethane/Ethylene Separation. *J. Mater. Chem. A* **2020**, *8*, 3613−3620.

(37) Sun, F.-Z.; Yang, S.-Q.; Krishna, R.; Zhang, Y.-H.; Xia, Y.-P.; Hu, T.-L. Microporous Metal-Organic Framework with a Completely Reversed Adsorption Relationship for C_2 Hydrocarbons at Room Temperature. *ACS Appl. Mater. Interfaces* **2020**, *12*, 6105−6111.

(38) Dang, L.-L.; Zhang, T.-T.; Chen, T.; Zhao, Y.; Gao, X.; Aznarez, F.; Ma, L.-F.; Jin, G.-X. Selective Synthesis and Structural Transformation of a 4-Ravel Containing four Crossings and Featuring Cp*Rh/Ir Fragments. *Angew. Chem., Int. Ed.* **2023**, *62*, No. e202301516.

(39) Lin, R. B.; Wu, H.; Li, L.; Tang, X. L.; Li, Z.; Gao, J.; Cui, H.; Zhou, W.; Chen, B. Boosting Ethane/Ethylene Separation within Isoreticular Ultramicroporous Metal-Organic Frameworks. *J. Am. Chem. Soc.* **2018**, *140*, 12940−12946.

(40) Dang, L.-L.; Zhang, T.-T.; Chen, T.; Zhao, Y.; Zhao, C.-C.; Aznarez, F.; Sun, K.-X.; Ma, L.-F. Coordination Assembly and NIR Photothermal Conversion of Cp*Rh-Based Supramolecular Topologies Based on Distinct Conjugated Systems. *Org. Chem. Front.* **2022**, *9*, 5505−5515.

(41) Ye, Y.; Xie, Y.; Shi, Y.; Gong, L.; Phipps, J.; Al-Enizi, A. M.; Nafady, A.; Chen, B.; Ma, S. A Microporous Metal-Organic Framework with Unique Aromatic Pore Surfaces for High Performance C_2H_6/C_2H_4 Separation. *Angew. Chem., Int. Ed.* **2023**, *20*, No. e202302564.

(42) Sheldrick, G. M. Crystal Structure Refinement with SHELXL. *Acta Crystallogr., Sect. C: Struct. Chem.* **2015**, *C71*, 3−8.

(43) Spek, A. L. Single-Crystal Structure Validation with the Program PLATON. *J. Appl. Crystallogr.* **2003**, *36*, 7−13.

(44) Canivet, J.; Fateeva, A.; Guo, Y.; Coasne, B.; Farrusseng, D. Water Adsorption in Mofs: Fundamentals and Applications. *Chem. Soc. Rev.* **2014**, *43*, 5594−5617.

(45) Yu, M.-H.; Zhang, P.; Feng, R.; Yao, Z.-Q.; Yu, Y.-C.; Hu, T.-L.; Bu, X.-H. Construction of a Multi-Cage-Based MOF with a Unique Network for Efficient CO_2 Capture. *ACS Appl. Mater. Interfaces* **2017**, *9*, 26177−26183.

(46) Zhang, Y.; Yang, L.; Wang, L.; Cui, X.; Xing, H. Pillar Iodination in Functional Boron Cage Hybrid Supramolecular Frameworks for High Performance Separation of light Hydrocarbons. *J. Mater. Chem. A* **2019**, *7*, 27560−27566.

(47) Fan, W.; Wang, Y.; Zhang, Q.; Kirchon, A.; Xiao, Z.; Zhang, L.; Dai, F.; Wang, R.; Sun, D. An Amino-Functionalized Metal-Organic Framework Based on a Rarely $Ba_{12}(COO)_{18}(NO_3)_2$ Cluster, for

Efficient $C_3/C_2/C_1$ Separation and Preferential Catalytic Performance. *Chem. − Eur. J.* **2017**, *24*, 2137−2143.

(48) Fan, W.; Wang, X.; Zhang, X.; Liu, X.; Wang, Y.; Kang, Z.; Dai, F.; Xu, B.; Wang, R.; Sun, D. Fine-Tuning the Pore Environment of the Microporous Cu-MOF for High Propylene Storage and Efficient Separation of Light Hydrocarbons. *ACS Cent. Sci.* **2019**, *5*, 1261−1268.

(49) Xu, Z.; Xiong, X.; Xiong, J.; Krishna, R.; Li, L.; Fan, Y.; Luo, F.; Chen, B. A Robust Th-Azole Framework for Highly Efficient Purification of C_2H_4 from a $C_2H_4/C_2H_2/C_2H_6$ Mixture. *Nat. Commun.* **2020**, *11*, 3163.

(50) Lysova, A. A.; Samsonenko, D. G.; Kovalenko, K. A.; Nizovtsev, A. S.; Dybtsev, D. N.; Fedin, V. P. A Series of Mesoporous Metal-Organic Frameworks with Tunable Windows Sizes and Exceptionally High Ethane over Ethylene Adsorption Selectivity. *Angew. Chem., Int. Ed.* **2020**, *59*, 20561−20567.

(51) Jiang, Y.; Hu, Y.; Luan, B.; Wang, L.; Krishna, R.; Ni, H.; Hu, X.; Zhang, Y. Benchmark Single-Step Ethylene Purification from Ternary Mixtures by a Customized Fluorinated Anion Embedded MOF. *Nat. Commun.* **2023**, *14*, 401.

(52) Sun, X.; Ma, Y.; Zhao, J.; Li, D.-S.; Li, G.; Zhang, L.; Liu, Y. Tuning the Gate Opening Pressure of a Flexible Doubly Interpenetrated Metal−Organic Framework through Ligand Functionalization. *Dalton Trans.* **2018**, *47*, 13158−13163.

(53) Jiang, C.; Wang, X.; Lu, K.; Jiang, W.; Xu, H.; Wei, X.; Wang, Z.; Ouyang, Y.; Dai, F. From Layered Structure to 8-Fold Interpenetrated MOF with Enhanced Selective Adsorption of C_2H_2/CH_4 and CO_2/CH_4. *J. Solid State Chem.* **2022**, *307*, No. 122881.

(54) Kim, D.; Jo, D.; Yoon, J. W.; Lee, S.-K.; Cho, K. H.; Bae, Y.-S.; Lee, U. H. High-Performance Adsorbent for Ethane/Ethylene Separation Selected through the Computational Screening of Aluminum-Based Metal−Organic Frameworks. *ACS Appl. Mater. Interfaces* **2022**, *14*, 43637−43645.

(55) Wu, X.-Q.; Zhang, P.-D.; Zhang, X.; Liu, J.-H.; He, T.; Yu, J.; Li, J.-R. Ethylene Purification in a Metal-Organic Framework over a Wide Temperature Range via Pore Confinement. *Green Energy Environ.* **2022**, DOI: 10.1016/j.gee.2022.03.015.

(56) Wang, Z.-Q.; Luo, H.-Q.; Wang, Y.-L.; Xu, M.-Y.; He, C.-T.; Liu, Q.-Y. Octanuclear Cobalt(II) Cluster-Based Metal−Organic Framework with Caged Structure Exhibiting the Selective Adsorption of Ethane over Ethylene. *Inorg. Chem.* **2021**, *60*, 10596−10602.

(57) Gao, Q.; Li, A.-L.; Chen, X.; Lu, N.; Zhang, Y.-M.; Chen, L.-Z. A Microporous Metal−Organic Framework with Triangular Channels for C_2H_6/C_2H_4 Adsorption Separation. *Sep. Purif. Technol.* **2021**, *276*, No. 119424.

(58) Liao, P.-Q.; Zhang, W.-X.; Zhang, J.-P.; Chen, X.-M. Efficient Purification of Ethene by an Ethane-Trapping Metal-Organic Framework. *Nat. Commun.* **2015**, *6*, 8697.

(59) Geng, S.; Lin, E.; Li, X.; Liu, W.; Wang, T.; Wang, Z.; Sensharma, D.; Darwish, S.; Andaloussi, Y. H.; Pham, T.; Cheng, P.; Zaworotko, M. J.; Chen, Y.; Zhang, Z. Scalable Room-Temperature Synthesis of Highly Robust Ethane-Selective Metal−Organic Frameworks for Efficient Ethylene Purification. *J. Am. Chem. Soc.* **2021**, *143*, 8654−8660.

(60) Myers, A. L.; Prausnitz, J. M. Thermodynamics of Mixed-Gas Adsorption. *AIChE J.* **1965**, *11*, 121−127.

(61) Chen, Y.; Wu, H.; Lv, D.; Shi, R.; Chen, Y.; Xia, Q.; Li, Z. Highly Adsorptive Separation of Ethane/Ethylene by an Ethane-Selective MOF MIL-142A. *Ind. Eng. Chem. Res.* **2018**, *57*, 4063−4069.

(62) Yang, L.; Yan, L.; Niu, W.; Feng, Y.; Fu, Q.; Zhang, S.; Zhang, Y.; Li, L.; Gu, X.; Dai, P.; Liu, D.; Zheng, Q.; Zhao, X. Adsorption in Reversed Order of C_2 Hydrocarbons on an Ultramicroporous Fluorinated Metal-Organic Framework. *Angew. Chem., Int. Ed.* **2022**, *61*, No. e202204046.

(63) Cao, J.-W.; Mukherjee, S.; Pham, T.; Wang, Y.; Wang, T.; Zhang, T.; Jiang, X.; Tang, H.-J.; Forrest, K. A.; Space, B.; Zaworotko, M. J.; Chen, K.-J. One-Step Ethylene Production from a Four-Component Gas Mixture by a Single Physisorbent. *Nat. Commun.* **2021**, *12*, 6507.

(64) Chen, C. X.; Wei, Z. W.; Pham, T.; Lan, P. C.; Zhang, L.; Forrest, K. A.; Chen, S.; Al-Enizi, A. M.; Nafady, A.; Su, C. Y.; Ma, S. Nanospace Engineering of Metal−Organic Frameworks through Dynamic Spacer Installation of Multifunctionalities for Efficient Separation of Ethane from Ethane/Ethylene Mixtures. *Angew. Chem., Int. Ed.* **2021**, *60*, 9680−9685.

(65) Krishna, R. Screening Metal−Organic Frameworks for Mixture Separations in Fixed-Bed Adsorbers using a Combined Selectivity/Capacity Metric. *RSC Adv.* **2017**, *7*, 35724−35737.

(66) Krishna, R. Methodologies for Screening and Selection of Crystalline Microporous Materials in Mixture Separations. *Sep. Purif. Technol.* **2018**, *194*, 281−300.

(67) Krishna, R. Metrics for Evaluation and Screening of Metal−Organic Frameworks for Applications in Mixture Separations. *ACS Omega* **2020**, *5*, 16987−17004.

Supplementary Information

Ultramicroporous Metal−Organic Framework with Inert Pore Surfaces for Inversed Separation of Ethylene from C_2 Hydrocarbons Mixtures

Hai-Yu Duan,[a] Xiu-Yuan Li,*[a] Rajamani Krishna[b] and Chaozheng He*[a]

[a]Shaanxi Key Laboratory of Optoelectronic Functional Materials and Devices, School of Materials Science and Chemical Engineering, Xi'an Technological University, Xi'an, 710021, P. R. China.

E-mail: lixiuyuan@xatu.edu.cn; hecz2019@xatu.edu.cn

[b]Van 't Hoff Institute for Molecular Sciences, University of Amsterdam, Science Park 904, 1098 XH Amsterdam, The Netherlands.

Table S1 Physical properties of C_2H_2, C_2H_4, and C_2H_6

Molecular formula	C_2H_2	C_2H_4	C_2H_6
Melting point (K)	189.1	103.9	89.8
Boiling point (K)	189.3	169.4	184.4
Critical temperature (K)	308.3	282.6	305.4
Critical pressure (MPa)	6.191	5.076	4.884
Molecular dimension (Å^3)	3.32×3.34×5.70	3.28×4.18×4.84	3.81×4.08×4.82
Polarizability ×10^{-25} (cm^3)	33.3-39.3	42.52	44.3-44.7
Quadrupole moment ×10^{-26} (esu cm^2)	7.2	1.5	0.65
Kinetic diameter (Å)	3.3	4.163	4.443

Table S2 Crystal Data and Structure Refinement for **1**.

Complex	**1**
Molecular Formula	$C_{54}H_{58}Co_3N_6O_{25}$
Formula Weight	1367.86
Temperature (K)	170.00
Crystal System	Cubic
Space Group	$P\bar{4}3n$
a (Å)	21.5197(3)
b (Å)	21.5197(3)
c (Å)	21.5197(3)
α (°)	90°
β (°)	90°
γ (°)	90°
V (Å^3)	9965.7(4)
Z	8
Dc (g·cm^{-3})	1.387
F(000)	4200
Reflections collected	28162
Goodness-of-fit on F^2	1.056
$R_1{}^a[I>2\sigma(I)]$	0.0683
w$R_2{}^b[I>2\sigma(I)]$	0.1987

$^aR_1 = \Sigma||F_o| - |F_c||/\Sigma|F_o|$. $^b\mathrm{w}R_2 = [\Sigma w(F_o{}^2 - F_c{}^2)^2/\Sigma w(F_o{}^2)^2]^{1/2}$

Table S3 Selected bond distances (Å) and angles (°) for **1**.

Co(1)-O(1)	2.071(7)	Co(1)-O(2)#1	2.137(7)
Co(1)-O(3)#2	2.077(6)	Co(1)-O(4)#3	2.133(7)
Co(1)-O(6)	2.0528(18)	Co(1)-N(1)	2.154(8)

Symmetry transformations used to generate equivalent atoms: #1 y,-z+1,-x+1; #2 x-1/2,z-1/2,y+1/2; #3 -y+1/2,x-1/2,-z+3

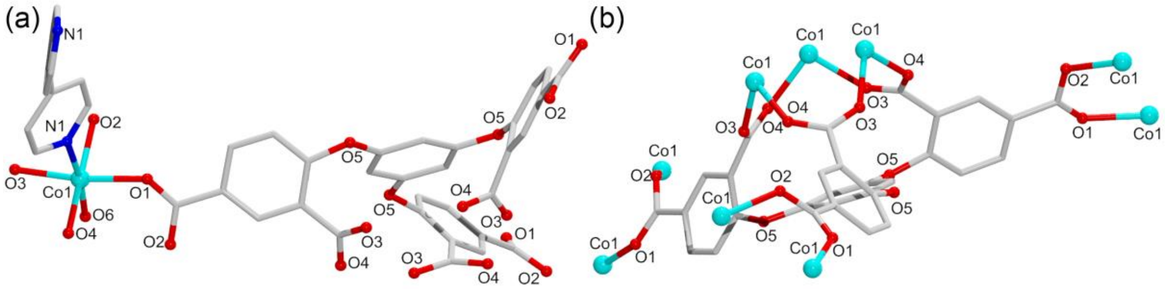

Figure S1. (a) Coordination environment of Co^{2+} ion in **1**; (b) Coordination environment of H_6tipa in **1**.

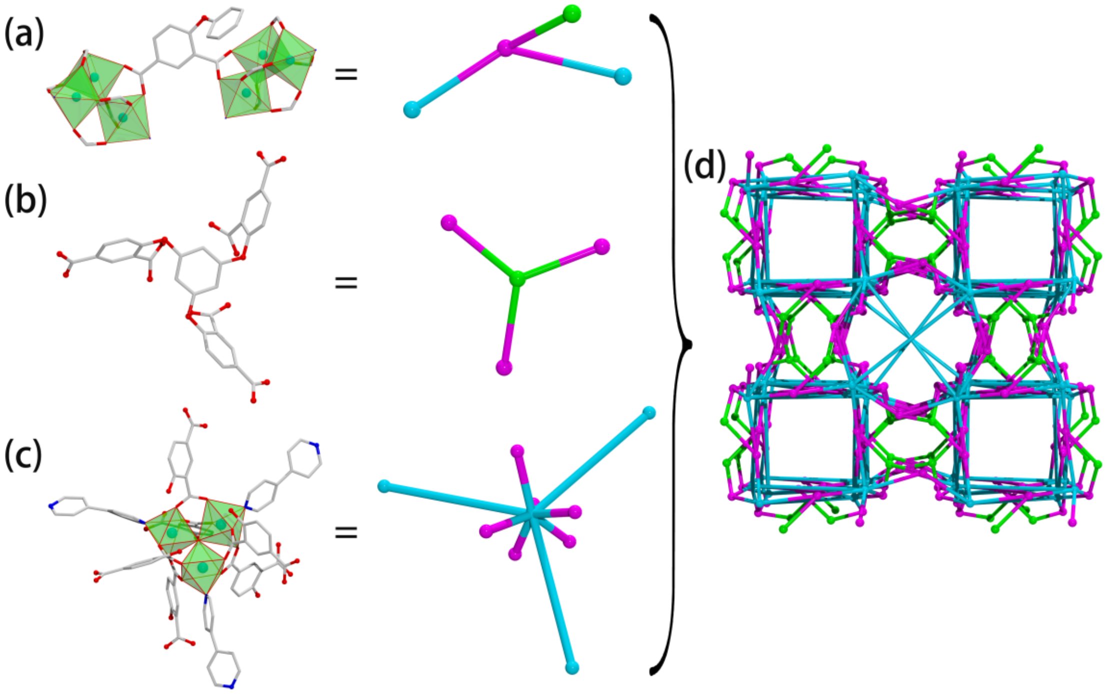

Figure S2. (a-c) Ball-and-stick and schematic representations of 3-connected nodes and 9-connected node, respectively. (d) Schematic representation of a trinodal (3,3,9)-connected network.

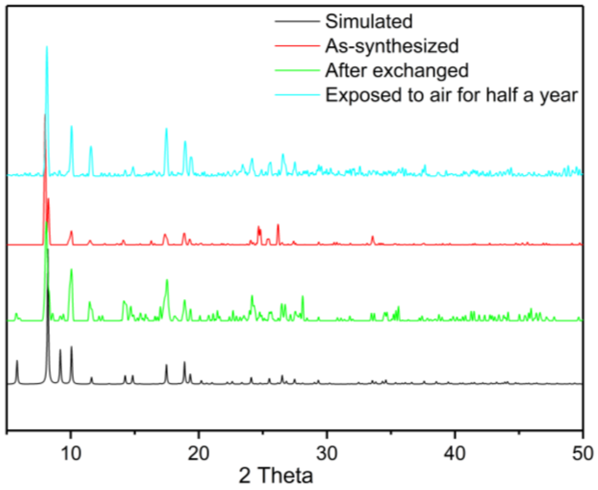

Figure S3. PXRD patterns for as-synthesized, after-exchanged and exposed to air for half a year of **1**.

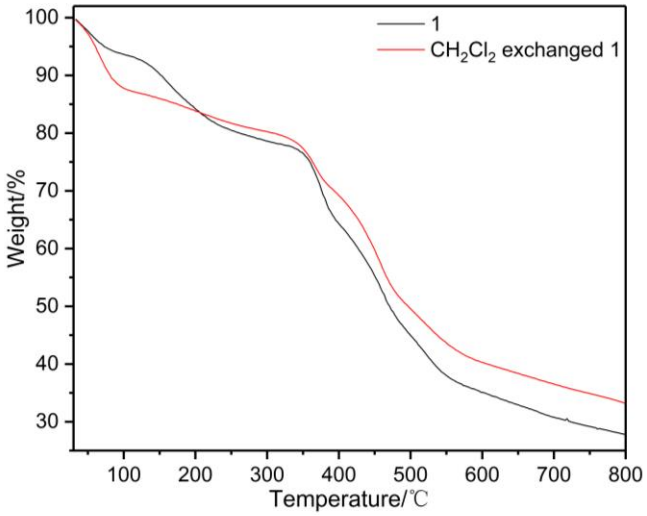

Figure S4. TGA curves for as-synthesized and after CH_2Cl_2 exchanged samples of **1**.

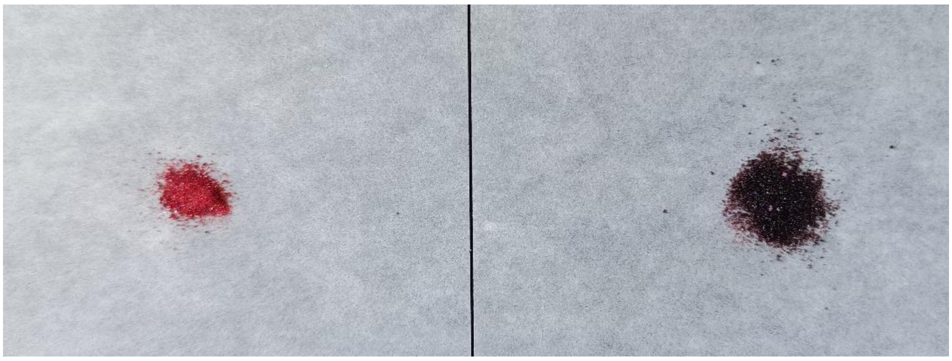

Figure S5. As-synthesized samples of **1** (left) and desolvated samples of **1** (right).

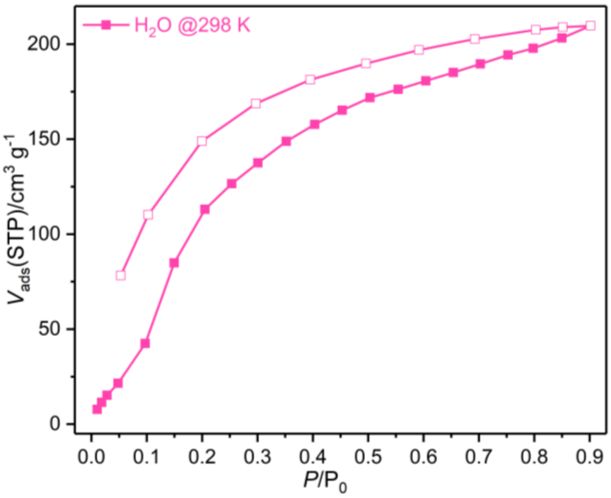

Figure S6. Water adsorption and desorption isotherm of **1a** at 298 K.

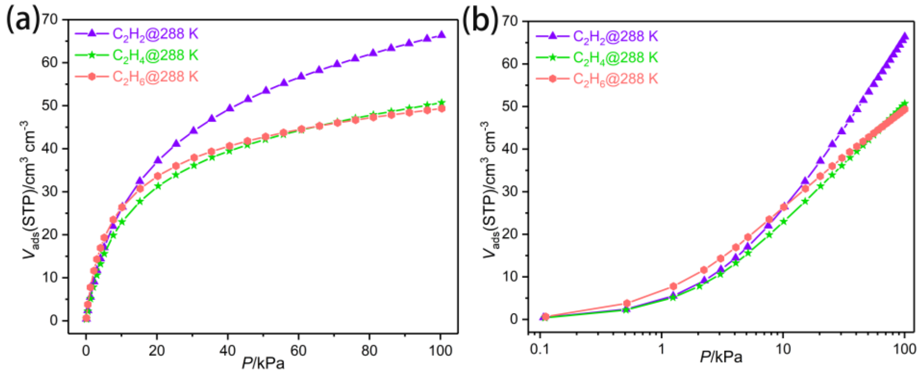

Figure S7. Gas sorption isotherms for C$_2$ hydrocarbons at 288 K.

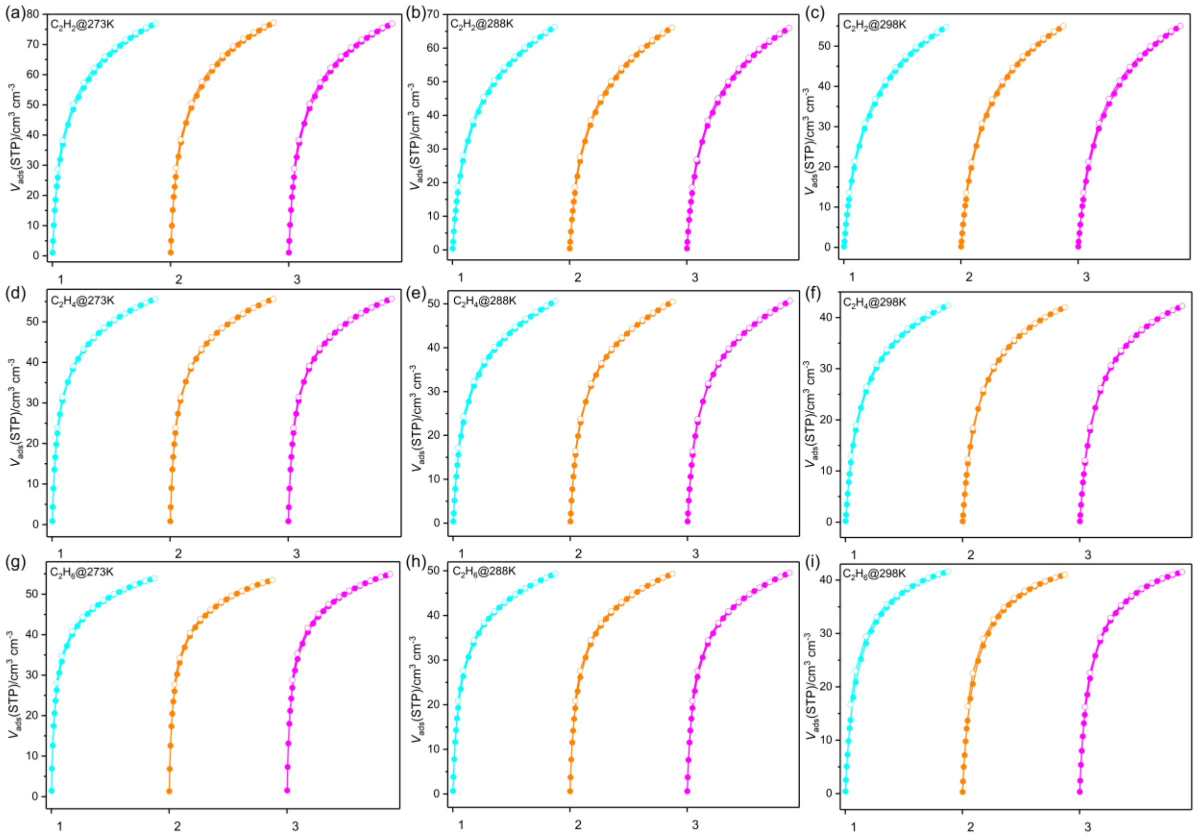

Figure S8. Cyclic gas sorption isotherms for C$_2$ hydrocarbons at (a), (d), (g) 273 K, (b), (e), (h) 288 K and (c), (f), (i) 298K.

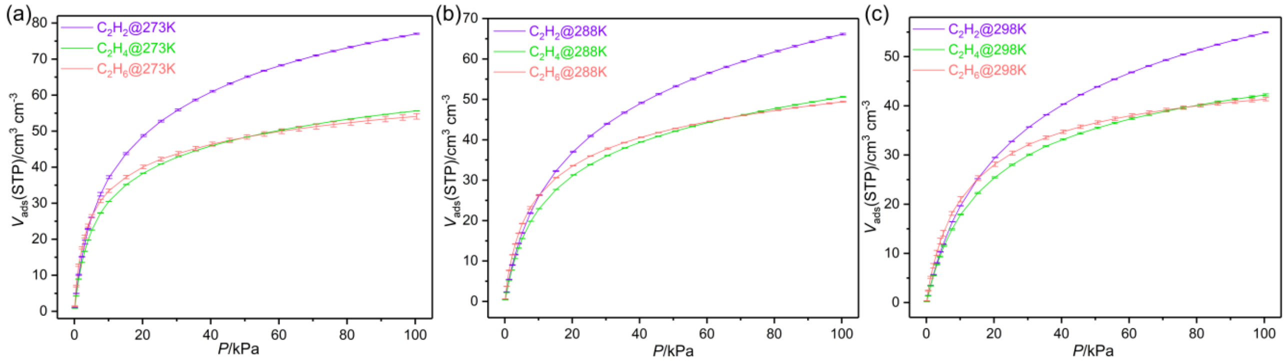

Figure S9. Error analysis of C$_2$ hydrocarbon at (a) 273 K, (b) 288 K and (c) 298 K.

Calculation of Sorption Heat using Virial 2 Model

$$\ln P = \ln N + 1/T \sum_{i=0}^{m} a_i N^i + \sum_{i=0}^{n} b_i N^i \qquad Q_{st} = -R \sum_{i=0}^{m} a_i N^i$$

The above virial expression was used to fit the combined isotherm data for **1a** at 298 K, where *P* is the pressure, *N* is the adsorbed amount, *T* is the temperature, a_i and b_i are virial coefficients, and *m* and *N* are the number of coefficients used to describe the isotherms. Q_{st} is the coverage-dependent enthalpy of adsorption and *R* is the universal gas constant.

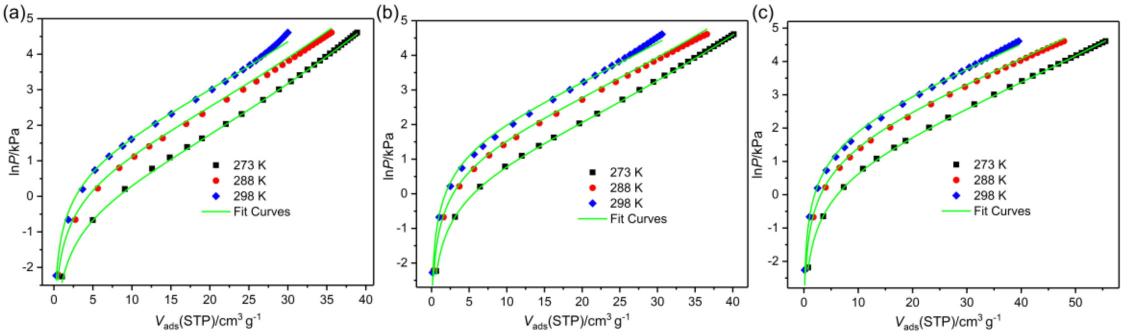

Figure S10. (a) C_2H_6, (b) C_2H_4 and (c) C_2H_2 adsorption isotherms of **1a** with fitting by Virial 2 model.

Table S4 Parameters obtained from the Virial 2 model fitting of the single-component adsorption isotherms at 298 K.

	C_2H_6	C_2H_4	C_2H_2
a0	-4482.39984	-4047.95268	-4228.31485
a1	9.34792	7.07374	8.29308
a2	0.37417	0.29991	0.08261
b0	13.92107	12.92457	13.4647
Chi^2	9.176E-03	8.046E-03	5.769E-03
R^2	0.997	0.998	0.998

Calculation of Sorption Heat using Clausius-Clapeyron Equation

The experimental isotherm data for pure C2-hydrocarbon were fitted using a Langmuir-Freundlich (L-F) model:

$$q = \frac{a*b*p^c}{1+b*p^c}$$

Where *q* and *P* are adsorbed amounts and the pressure of component *i*, respectively.

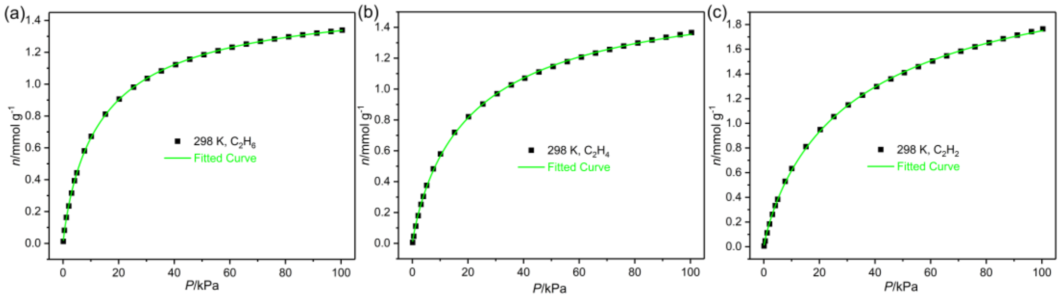

Figure S11. Adsorption isotherms of **1a** fitting by L-F model.

Table S5 Parameters obtained from the Langmuir-Freundlich fitting of the single-component adsorption isotherms.

298 K	C_2H_6	C_2H_4	C_2H_2
a	1.57862	1.71937	2.47231
b	0.09439	0.06408	0.04581
c	0.88335	0.88113	0.86135
Chi^2	1.133E-05	5.452E-05	8.078E-05
R^2	1.000	1.000	1.000

The isosteric heat of adsorption (Q_{st}) can be calculated via the Clausius-Clapeyron equation:

$$Q_{st} = -R\left[\frac{\partial lnp}{\partial(1/T)}\right]_N \qquad (E1)$$

where p is the pressure, T is the temperature, N is the amount adsorbed, R is the universal gas constant. Integrating equation (E1) gives:

$$(\ln p)_N = -\left(\frac{Q_{st}}{R}\right)\left(\frac{1}{T}\right) + C \quad (E2)$$

where C is a constant. Here an isotherm is first fitted to a high-order polynomial equation to obtain an expression for N as a function of p. Then the values of p at a given N for each T can be interpolated from the fitted equation. At each given N, the isostere plot of (ln p)$_N$ as a function of (1/T), which is obtained from linear regression, matches with the form of equation (E2), and therefore the Q_{st} values can be computed from the slopes of the isostere plot.

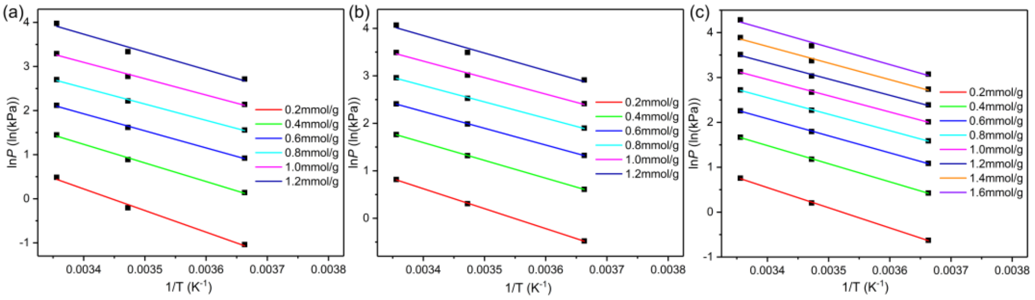

Figure S12. Linear relationship between ln*P* and 1/*T* for (a) C_2H_6, (b) C_2H_4 and (c) C_2H_2.

Gas Selectivity Prediction via IAST

The experimental isotherm data for pure C2-hydrocarbon were fitted using a dual Langmuir-Freundlich (L-F) model:

$$q = \frac{a_1 * b_1 * p^{c1}}{1 + b_1 * p^{c1}} + \frac{a_2 * b_2 * p^{c2}}{1 + b_2 * p^{c2}}$$

Where *q* and *P* are adsorbed amounts and the pressure of component *i*, respectively.

The adsorption selectivities for binary mixtures defined by

$$S_{i/j} = \frac{x_i * y_j}{x_j * y_i}$$

were respectively calculated using IAST. Where x_i is the mole fraction of component *i* in the adsorbed phase and y_i is the mole fraction of component *i* in the bulk.

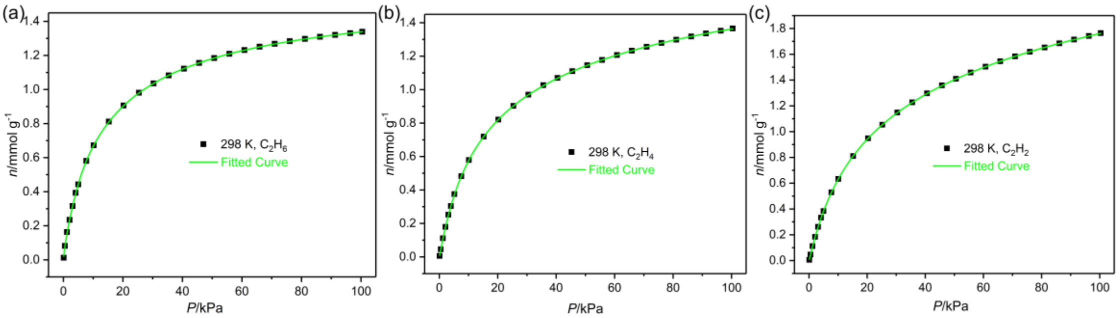

Figure S13. Adsorption isotherms of **1a** fitting by dual L-F model.

Table S6 Parameters obtained from the dual Langmuir-Freundlich fitting of the single-component adsorption isotherms.

298 K	C_2H_6	C_2H_4	C_2H_2
a1	0.03009	0.89496	1.16086
b1	0.00228	0.09147	0.07187

c1	3.78086	1.05394	1.02086
a2	1.57029	0.96401	1.60733
b2	0.0942	0.01588	0.00955
c2	0.86222	0.95055	0.97014
Chi^2	6.408E-06	1.723E-06	1.915E-06
R^2	1.000	1.000	1.000

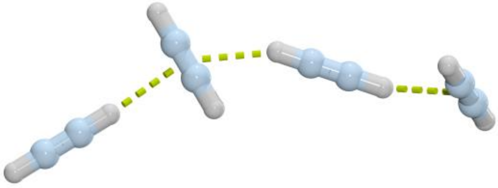

Figure S14. Packing of C_2H_2 molecules in channels at 100 kPa and 298 K.

Transient Breakthrough Simulations

Transient breakthrough simulations were carried out using the methodology described in earlier publications.[1-5] The following mixtures were simulated:

binary 50/50 C_2H_4/C_2H_6 mixtures

binary 90/10 C_2H_4/C_2H_6 mixtures

ternary 89/10/1 $C_2H_4/C_2H_6/C_2H_2$ mixtures

For these simulations we choose: length of packed bed, L = 0.3 m; cross-sectional area, A = 1 m^2; volumetric flow rate of gas mixture at the entrance to the bed, $Q_0 = 0.04$ m^3 s^{-1}; voidage of the packed bed, ε = 0.4. The total volume of the bed is $V_{bed} = LA$. The volume of MOF used in the simulations is $V_{ads} = LA(1-\varepsilon)$. It is important to note that the volume of adsorbent, V_{ads}, includes the pore volume of the adsorbent material. If ρ is the crystal framework density, the mass of the adsorbent in the bed is $m_{ads} = (1-\varepsilon)\times(L \text{ m})\times(A \text{ m}^2)\times(\rho \text{ kg m}^{-3})$ kg. The dimensionless concentrations in the exit, c_i/c_{i0} are plotted as a function of the parameter $\frac{(Q_0 = \text{flow rate L s}^{-1})\times(\text{time in s})}{(\text{kg MOF packed in tube})} = \frac{Q_0 t}{m_{ads}} = \text{L kg}^{-1}$.

c_i molar concentration of species i, mol m^{-3}

c_{i0}	molar concentration of species *i* in fluid mixture at inlet, mol m^{-3}
Q_0	volumetric flow rate of gas mixture, m^3 s^{-1}
L	length of packed bed adsorber, m
m_{ads}	mass of adsorbent in packed bed, kg
t	time, s
T	absolute temperature, K
ε	voidage of packed bed, dimensionless
ρ	framework density, kg m^{-3}

GCMC Simulation Methodology

Grand Canonical Monte Carlo (GCMC) simulations were performed to assess adsorption performance. The 2×2×2 supercell was used for the simulations. The partial charges for atoms of the framework were derived from QEq method.[6] All the parameters for atoms of MOF except metal atoms were modeled with the DREIDING forcefield, while metal atoms were modeled with the universal forcefield.[7,8] The LJ potential parameters for guests were taken from the Optimized Potentials for Liquid Simulations-All Atom (OPLS-AA) force field.[9] A cutoff distance of 10.5 Å was used for LJ interactions, and the Coulombic interactions were calculated by using Ewald summation. For each run, the 5×10^6 equilibration steps, 5×10^6 production steps were employed.

Table S7 The partial charges for atoms of the framework.

Atoms	Charges	Atoms	Charges
Co1	1.236422	H6A	0.1966151
O1	-0.5497197	C7	-0.2122157
O2	-0.5309756	H7	0.1416356
O3	-0.5241014	C8	0.526795
O4	-0.5717756	C9	0.2056871
O5	-0.5834603	C10	-0.078951
O6	-0.5438796	H10	0.1181861
H6	0.2732708	C11	0.02673708
N1	-0.2540275	H11	0.1450907
C1	0.5537508	C12	-0.1562251

C2	-0.003346623	H12	0.1200169
C3	-0.1856025	C13	0.02374584
H3	0.1350813	C14	-0.1435138
C4	0.01159217	H14	0.1274724
C5	0.2757868	C15	0.02096594
C6	-0.1145076	H15	0.1330442

References

(1) Krishna, R. The Maxwell-Stefan Description of Mixture Diffusion in Nanoporous Crystalline Materials. *Microporous Mesoporous Mater.* **2014**, *185*, 30-50.

(2) Krishna, R. Methodologies for Evaluation of Metal-Organic Frameworks in Separation Applications. *RSC Adv.* **2015**, *5*, 52269-52295.

(3) Krishna, R. Screening Metal-Organic Frameworks for Mixture Separations in Fixed-Bed Adsorbers using a Combined Selectivity/Capacity Metric. *RSC Adv.* **2017**, *7*, 35724-35737.

(4) Krishna, R. Methodologies for Screening and Selection of Crystalline Microporous Materials in Mixture Separations. *Sep. Purif. Technol.* **2018**, *194*, 281-300.

(5) Krishna, R. Metrics for Evaluation and Screening of Metal-Organic Frameworks for Applications in Mixture Separations. *ACS Omega* **2020**, *5*, 16987−17004.

(6) Rappe, A. K.; Goddard, W. A. Charge Equilibration for Molecular Dynamics Simulations. *J. Phys. Chem.* **1991**, *95*, 3358-3363.

(7) Mayo, S. L.; Olafson, B. D.; Goddard, W. A. DREIDING: a Generic Force Field for Molecular Simulations. *J. Phys. Chem.* **1990**, *94*, 8897-8909.

(8) Rappe, A. K.; Casewit, C. J.; Colwell, K. S.; Goddard, W. A.; Skiff, W. M. UFF, a Full Periodic Table Force Field for Molecular Mechanics and Molecular Dynamics Simulations. *J. Am. Chem. Soc.* **1992**, *114*, 10024-10035.

(9) Jorgensen, W. L.; Maxwell, D. S.; Tirado-Rives, J. Development and Testing of the OPLS All-Atom Force Field on Conformational Energetics and Properties of Organic Liquids. *J. Am. Chem. Soc.* **1996**, *118*, 11225-11236.